photonics

MDPI

Article

Toward a Dual-Input Feedback Speckle Imaging Framework Under Multiple Light Sources in the Presence of Ambient Illumination

Anqi Leng [1], Guangmang Cui [1,2,3,*], Yan Chen [1], Jianhua Mo [1], Weize Cui [1], Lize Fang [1], Zhanhong Liu [1] and Jufeng Zhao [1,2,3]

[1] School of Electronics and Information, Hangzhou Dianzi University, Hangzhou 310018, China; 23150905@hdu.edu.cn (A.L.); 24041710@hdu.edu.cn (Y.C.); 252040324@hdu.edu.cn (J.M.); 232040112@hdu.edu.cn (W.C.); 25041424@hdu.edu.cn (L.F.); 242040124@hdu.edu.cn (Z.L.); dabaozjf@hdu.edu.cn (J.Z.)

[2] Zhejiang Key Laboratory of Optoelectronic Intelligent Imaging and Aerospace Sensing, Hangzhou Dianzi University, Hangzhou 310018, China

[3] Shaoxing Optoelectronics Research Center, Shaoxing 312030, China

* Correspondence: cuigm@hdu.edu.cn; Tel.: +86-571-86919029

Abstract

Recovering high-quality images from low-quality speckle patterns remains a core challenge in scattering imaging, especially under narrowband illumination with ambient light interference and broadband illumination. This paper proposes a dual-input synchronous transmission architecture: after Correction-Smoothing-Phase Optimization (CSPO) preprocessing, two data streams are parallel-fed into Phase-Aligned Coherent Summation (PACS) for efficient and high-precision reconstruction with adaptive fusion, breaking the single-path limitation of traditional methods and balancing imaging efficiency and quality. Additionally, an adaptive enhancement factor feedback mechanism is designed for Median-Unsharp Sharpening Enhancement (MUSE) to dynamically adjust Median Filtering (MF) and Unsharp Masking (USM) parameters, achieving adaptive balance between noise suppression and detail enhancement and improving robustness under extreme lighting. In PACS, a dynamic reference update mechanism is introduced, combined with fixed amplitude to realize iterative phase optimization, effectively suppressing speckle noise and boosting the signal-to-noise ratio of reconstructed images. Experimental results show that the proposed method achieves favorable restoration performance even at a SNR of −8.7 dB under narrowband and broadband illumination with spectral bandwidths of 100 nm, 200 nm, and 280 nm (FWHM), and significantly improves image quality in unknown scattering media, showing great potential for robust speckle reconstruction.

Keywords: Speckle Correlation Imaging (SCI); multi-light source; ambient light; dual-input mechanism

Check for updates

Received: 9 April 2026
Revised: 22 May 2026
Accepted: 3 June 2026
Published: 5 June 2026

Copyright: © 2026 by the authors. Licensee MDPI, Basel, Switzerland. This article is an open access article distributed under the terms and conditions of the Creative Commons Attribution (CC BY) license.

1. Introduction

During the propagation of light through strongly scattering media, photons undergo multiple scattering events, which makes it impossible to accurately extract target information on the observation plane. Therefore, recovering clear images of objects hidden behind strongly scattering media has long been a core challenge in the field of scattering imaging. Through the relentless efforts of researchers, speckle imaging technology has gradually matured. Today, existing research results include wavefront shaping, transmission matrix, deep learning (DL), and point spread function deconvolution. The proposal of the Optical

Memory Effect (OME) in 1988 provided a strong impetus for the development of speckle imaging. Speckle Correlation Imaging (SCI) based on the OME mainly relies on phase retrieval algorithms to achieve complete reconstruction of target information. Compared with traditional imaging methods, SCI eliminates the need for complex wavefront modulation and features non-invasiveness and high imaging speed. It has thus become an important research direction in this field [1]. The core principle of SCI is based on the fact that the autocorrelation function of a speckle pattern contains the Fourier transform spectrum of the object. By performing autocorrelation analysis on speckle images, the spatial information of the object can be extracted, enabling object reconstruction [2]. However, the practical application of SCI is often limited by ambient light interference and broadband lighting conditions. To address this, Yuan et al. achieved dynamic imaging under low signal-to-noise ratio (SNR) conditions by reconstructing the Optical Transfer Function (OTF) and combining it with deconvolution technology [3]. Additionally, Lu et al. implemented non-invasive imaging under white light illumination using an improved iterative algorithm, though minor distortions still existed in the reconstruction results [4]. Li et al. successfully achieved imaging under ambient light interference by eliminating background noise in the autocorrelation domain [5]. Miao et al. proposed an adaptive windowing method to achieve efficient non-line-of-sight imaging under strong ambient light and low SNR [6]. Qiao et al. realized high dynamic range imaging by using forward scattering [7], and Liu et al. achieved single-shot broadband scattering imaging through frequency-domain optimization [8]. With the development of deep learning, Tang et al. proposed the TransFNet network, which combines physical priors with Transformer to improve the generalization ability and reconstruction accuracy of speckle correlation imaging [9]. Although these methods achieve satisfactory reconstruction performance, they fail to deliver consistent and universal results across different scenarios, and their robustness still needs to be further improved.

Noise in speckle images degrades imaging quality and affects the accuracy of phase retrieval [6]. Since optical detectors can only record light intensity instead of phase, various phase retrieval algorithms have been developed, including the alternating projection–based GS algorithm that easily converges to local minima [10,11], PhaseLift with strong stability and noise robustness but high computational complexity [12], and coherent averaging that suppresses noise yet cannot address phase incoherence under ambient light or broadband illumination [13]. Meanwhile, conventional image enhancement methods [14] rely on spatial-domain processing or frequency-domain transforms such as Fourier Transform (FT), Discrete Cosine Transform (DCT), and Discrete Wavelet Transform (DWT), which can improve contrast and edge details but fail to balance noise suppression and detail preservation for speckle images with salt-and-pepper noise and uneven illumination, making them unsuitable for SCI under extreme lighting conditions.

Reconstructed results of SCI under complex ambient light are generally plagued by salt-and-pepper noise and edge blurring, which severely degrade the visibility of microstructures and the accuracy of subsequent analysis, forming a core bottleneck restricting the practical application of SCI in complex light fields. To address this, we construct a unified dual-input feedback speckle imaging framework that breaks the limitations of traditional single-path algorithms. This framework achieves full-link robustness from preprocessing to reconstruction through the deep integration of adaptive enhancement and phase coherence optimization: in the preprocessing stage, CSPO integrates frequency-domain smooth correction and phase optimization logic to effectively eliminate uneven illumination and suppress low-frequency interference; MUSE acts as a precise front-end processor, suppressing salt-and-pepper noise while enhancing edge details without significantly amplifying background noise, which directly sharpens the peak of the cross-correlation

function, improves image matching accuracy, and thus strengthens the robustness of subsequent registration and PACS coherent reconstruction. In the core reconstruction stage, we design a dual-input synchronous transmission architecture: after unified preprocessing by CSPO, one data stream is directly fed into PACS for fast phase retrieval, while the other is fed into PACS after MUSE adaptive enhancement for high-precision reconstruction. Finally, PACS achieves phase consistency calibration through cross-correlation displacement estimation and circular alignment and completes iterative phase optimization and information fusion combined with the fixed amplitude obtained from multi-block power spectrum averaging.

The main contributions of our work are summarized as follows:

- A unified speckle imaging framework is proposed, with a novel dual-input synchronous transmission architecture. After unified CSPO preprocessing, two data channels are parallel-fed into PACS for efficient and high-precision reconstruction, respectively, with result fusion in PACS. It breaks the single-path limitation of traditional methods, balancing imaging efficiency and reconstruction quality under complex ambient light conditions.
- An adaptive enhancement factor feedback device is designed for MUSE, which dynamically adjusts MF and USM enhancement factors according to real-time speckle image features. It breaks the fixed parameter limitation, realizes adaptive balance between noise suppression and detail enhancement, and improves the framework's robustness under extreme lighting.
- A dynamic reference update mechanism is designed in PACS, where the reconstructed result after each iteration replaces the initial reference block. Combined with fixed amplitude derived from power spectrum averaging, it realizes iterative optimization of phase accuracy, effectively suppressing random speckle noise and improving the signal-to-noise ratio of reconstructed images under complex scattering conditions.

2. Materials and Methods

2.1. Methods

Before introducing the proposed method, we first present the flowchart of this framework. The overall flowchart is illustrated in Figure 1:

2.1.1. Basis of Speckle Correlation

The theory of OME explains that even though speckle images are affected by noise and the Point Spread Function (PSF), the optical information of an object can still be recovered through the autocorrelation operation of speckle images [15]. The response PSF of a scattering imaging system blurs the image, and the speckle image $I(\vec{r})$ captured by the camera is the convolution of the object image $O(\vec{r})$ and the PSF $S(\vec{r})$, defined as

$$I(r) = O(r) * S(r) + N(r) \tag{1}$$

where the symbol $*$ denotes the 2D convolution operation, and N is the noise term. Image reconstruction often relies on spectral analysis, whose key step is to calculate autocorrelation to extract the Fourier spectrum of the object. According to the OME theory, the Fourier amplitude spectrum of the object can be obtained using the autocorrelation operator based on the Wiener–Khinchine theorem:

$$I(\vec{r}) \otimes I(\vec{r}) \approx \left[O(\vec{r}) \otimes O(\vec{r})\right] + N_B \tag{2}$$

where the symbol $\otimes$ represents the correlation operation, and N_B is the background noise in the autocorrelation domain. Since autocorrelation can only recover amplitude information,

a phase retrieval algorithm is further required to recover the missing Fourier phase for object image reconstruction.

The above theory applies to ideal experimental conditions, i.e., using narrowband incoherent light for illumination in a darkroom. If the light source condition is changed to broadband lighting or disturbed by ambient light, the noise term N in Equation (1) cannot be neglected. A group of the typical reconstruction results under different lighting conditions is shown in Figure 1. During the autocorrelation operation, this noise manifests as strong background noise that masks spectral information. At this point, the speckle image exhibits low contrast, which affects image quality. Notably, under ambient light interference, the reconstructed "H" appears visually widened. This is not a physical change in the target, but an artifact caused by reduced SNR and suppressed high-frequency edge information, leading to blurred contours [see Figure 2c]. In the following sections, we will improve the reconstruction effect by combining robust phase retrieval and denoising strategies.

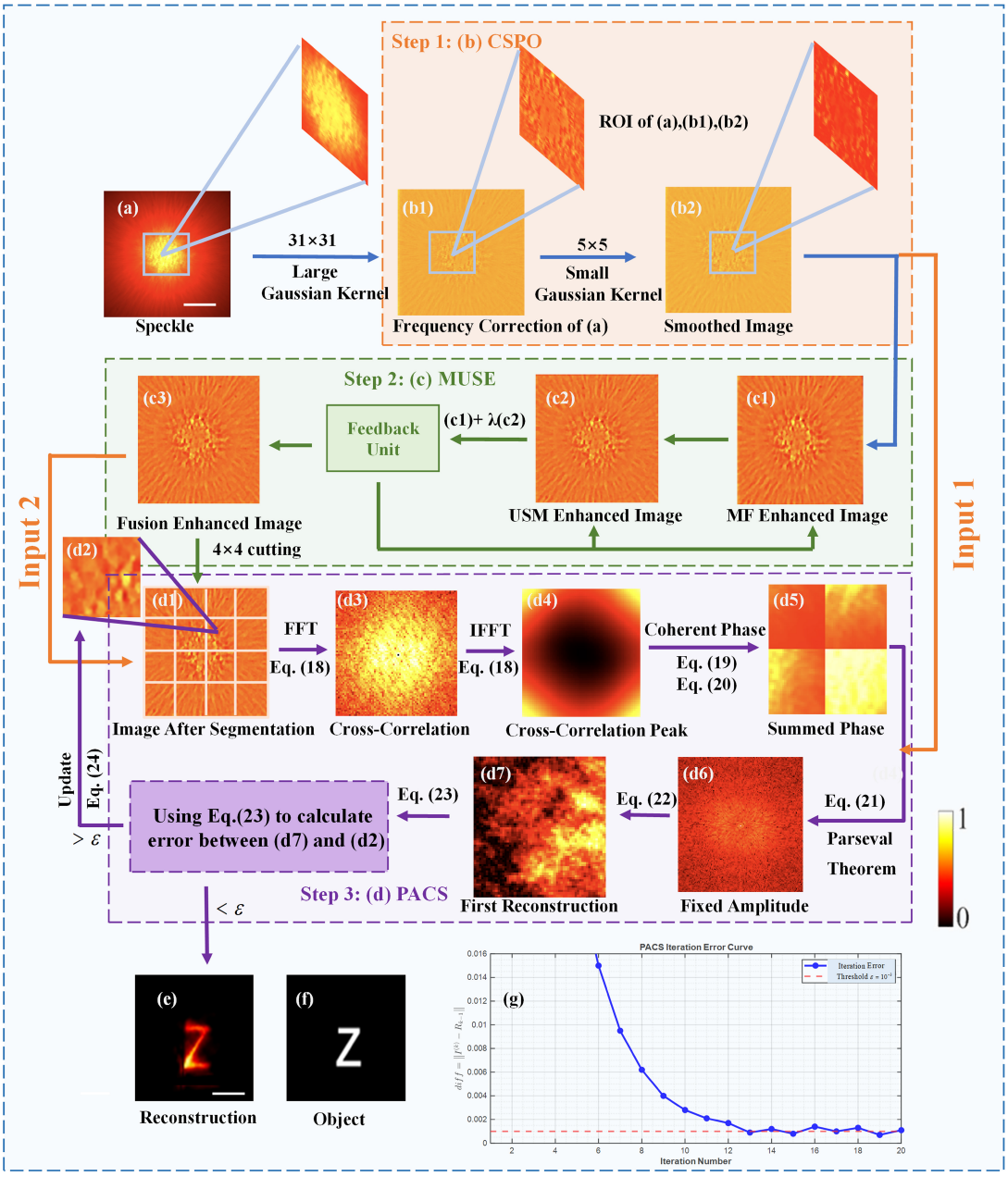


Figure 1. Flowchart of our method. (**a**) Speckle image. Step 1 (Section 2.1.2): (**b**) CSPO: (**b1**) Frequency correction of (**a**). (**b2**) Smoothed image. Step 2 (Section 2.1.3): (**c**) MUSE: (**c1**) MF-enhanced image.

(**c2**) USM-enhanced image. (**c3**) Fusion-enhanced image. Step 3 (Section 2.1.3): (**d**) PACS phase recovery method: (**d1**) Image after segmentation. (**d2**) Reference block. (**d3**) Cross-correlation after FFT. (**d4**) Cross-correlation peak after IFFT. (**d5**) Summed phase map. (**d6**) Fixed amplitude. (**d7**) First reconstruction. (**e**) Reconstruction of (**a**). (**f**) Object image. (**g**) Iteration error curve of our method. Input 1 to PACS is the output of CSPO. Input 2 is the CSPO-processed data, which is further processed by MUSE before being fed into PACS. The complete flow of the PACS iterative reconstruction mechanism is described in Algorithm 1. Scale bar: 281.28 μm.

Algorithm 1 Phase Signed Coherent Summit (PACS) Iterative Reconstruction

Input: Dual-input processed speckle image I, sub-speckle block parameters, max iterations K, tolerance ε
Initialization: Divide the processed image into N overlapping sub-speckle blocks: $B = \{B_1, B_2, \ldots, B_N\}$. Randomly select one sub-speckle block as the initial reference: $R_0 = B_{\text{rand}}$
1: for $k = 1$ to K do
2: for each $B_i \in B$ do
3: Compute cross-correlation with the current reference:
4: $C_i = \mathcal{F}^{-1}\{\mathcal{F}(B_i) \odot \mathcal{F}(R_{k-1})^*\}$ ← Equation (18)
5: $(\Delta x_i, \Delta y_i) = \text{argmax}(C_i)$
6: $B_i^{\text{align}} = \text{circshift}(B_i, [\Delta x_i, \Delta y_i])$ ← Equation (19)
7: end for
8: Coherent summation of all aligned sub-blocks:
9: $\phi_k = \frac{1}{N}\sum_{i=1}^{N} B_i^{\text{align}}$ ← Equation (20)
10: Compute fixed amplitude constraint (only in first iteration):
11: if $k == 1$ then
12: $\overline{P} = \frac{1}{N}\sum_{i=1}^{N} |\mathcal{F}(B_i)|^2$ ← Equation (21)
13: $A = \sqrt{\left|\mathcal{F}\left(\mathcal{F}^{-1}(\overline{P})\right)\right|}$ ← Equation (21)
14: end if
15: Synthesize frequency-domain signal:
16: $F_k = A \odot \exp(j \cdot \angle\mathcal{F}(\phi_k))$ ← Equation (22)
17: $I_k = \left|\mathcal{F}^{-1}(F_k)\right|$ ← Equation (22)
18: $\text{diff} = \|I_k - R_{k-1}\|_2$ ← Equation (23)
19: if diff $< \varepsilon$ then
20: break
21: end if
22: $R_k = \text{center}(I_k)$ ← Equation (24)
23: end for
Output: Reconstructed result O.

2.1.2. Dual-Input Mechanism

Speckle imaging relies on accurate phase alignment and coherent accumulation to achieve high-quality reconstruction. Nevertheless, traditional single-path reconstruction frameworks suffer from inherent conflicts among efficiency, accuracy and robustness. Input1 adopts a lightweight structure with low computational cost and shorter reconstruction time, yet it is limited in noise suppression and detail recovery. In contrast, Input2 utilizes complex iterative optimization to achieve superior reconstruction accuracy under ideal darkroom conditions, but it requires heavy computation and consumes much more runtime.

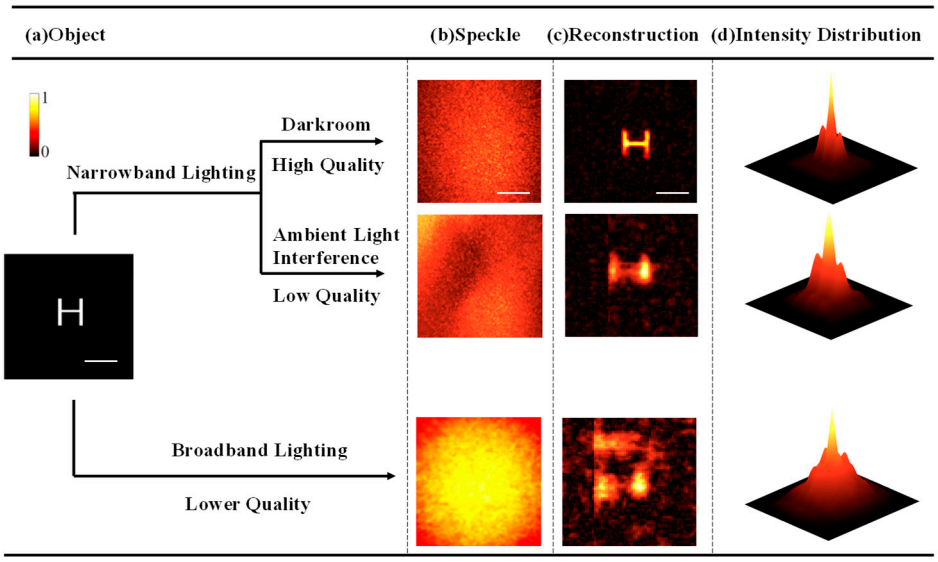


Figure 2. The reconstruction results under different lighting conditions. (**a**) Object image. (**b**) Speckle of (**a**). (**c**) Reconstruction of (**b**). (**d**) Energy intensity distribution of (**c**). Scale bar: 281.28 μm.

These two single-path schemes exhibit opposite and unstable performance in different scenarios. In the interference-free darkroom, Input2 delivers better imaging results than Input1. When confronted with non-uniform illumination and high-frequency environmental noise, however, the simple architecture of Input1 avoids noise amplification and maintains stable reconstruction. On the contrary, the elaborate iterative operations of Input2 will magnify noise and artifacts, resulting in severe degradation of imaging quality [see Figure 3]. Universal environmental interference in raw speckle images further restricts the practical applicability of single-path methods.

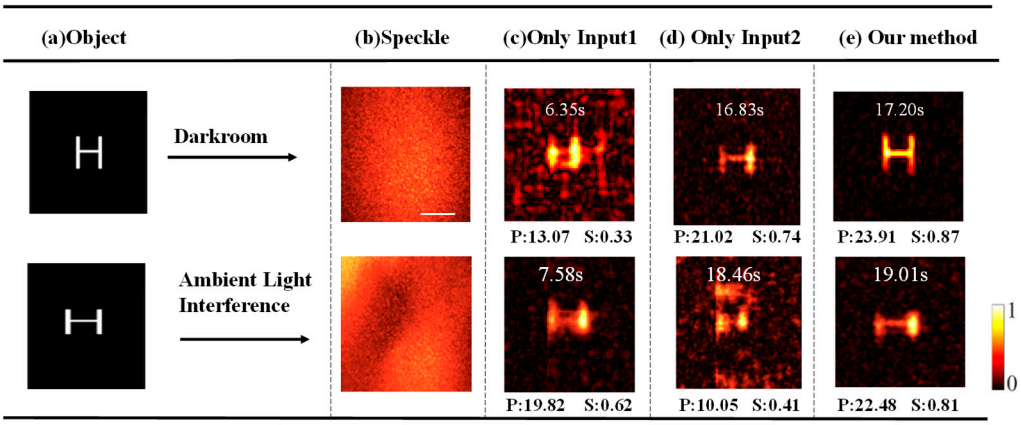


Figure 3. The reconstruction results under different inputs. (**a**) Object image. (**b**) Speckle of (**a**). (**c**) Reconstruction of only input 1. (**d**) Reconstruction of only input 2. (**e**) Reconstruction of our method. For each reconstructed image, the quantitative metrics P (PSNR, in dB) and S (SSIM) are provided below. Scale bar: 281.28 μm.

With only a moderate increase in time cost, the proposed dual-input method integrates the complementary advantages of the two branches. It achieves stable and high-quality reconstruction in both darkroom and noise-disturbed environments, effectively overcoming the inherent drawbacks of conventional single-path frameworks.

To break through this bottleneck at the architectural level, this paper proposes a dual-input parallel transmission architecture that decouples the objectives of high-efficiency imaging and high-precision reconstruction into separate channels. Meanwhile, CSPO

is introduced as a unified preprocessing front-end to provide high-quality and phase-consistent speckle data for both input channels.

Specifically, non-uniform brightness in speckle images caused by uneven light intensity destroys the phase consistency among sub-speckles, thus reducing reconstruction accuracy. The CSPO first eliminates non-uniform illumination via frequency-domain flat-field correction, which separates and removes low-frequency background components while retaining high-frequency speckle features in the frequency domain. We establish the following signal decomposition model [16]:

$$I(x,y) = S(x,y) \cdot B(x,y) \tag{3}$$

where $I(x,y)$ is the intensity of the original speckle image, $S(x,y)$ is the pure speckle signal, and $B(x,y)$ is the non-uniform illumination background. The correction formula is as follows:

$$I_{corr}(x,y) = \frac{I(x,y)}{B(x,y)} = S(x,y) \tag{4}$$

Electronic noise and environmental interference of the imaging system exist in the image in the form of high-frequency fluctuations, which mask the true phase information of the speckles and lead to blurred details and unstable convergence during iterative reconstruction. Gaussian smoothing is used to perform weighted averaging on the image because the central pixel of the image has a higher weight, while the surrounding pixels have lower weights, which in turn smooths high-frequency fluctuations and retains low-frequency or intermediate-frequency information. A small kernel size and small standard deviation are selected to balance noise reduction and image detail preservation. The spatial-domain convolution kernel of the Gaussian filter is [15]:

$$G(x,y) = \frac{1}{2\pi\sigma^2} \cdot e^{-\frac{x^2+y^2}{2\sigma^2}} \tag{5}$$

where $G(x,y)$ is the filter weight value, σ is the parameter controlling the blurring degree, $\frac{1}{2\pi\sigma^2}$ is the coefficient ensuring the total weight is 1, and $e^{-\frac{x^2+y^2}{2\sigma^2}}$ is the expression defining higher weights at the center, lower weights at the edges, and an exponential decay with distance.

After the unified CSPO preprocessing, the corrected and smoothed speckle data are fed into the dual-input parallel transmission architecture. One data branch is designed for high-efficiency reconstruction, adopting lightweight phase retrieval and fast coherent accumulation with low computational costs, ensuring real-time performance. The other branch targets high-precision reconstruction, using refined iterative phase optimization and multi-scale coherent accumulation to further correct phase errors and residual disturbances based on the preliminary results, improving detail recovery. The two branches are input into PACS in parallel, where result fusion is performed internally to finally output reconstructed images with both efficiency and accuracy.

This design breaks the single-path limitation of traditional methods and achieves a synergistic improvement of imaging efficiency and reconstruction quality under complex ambient light conditions. Meanwhile, the unified preprocessing of CSPO provides stable data support for the dual-input architecture, avoiding performance degradation between the two paths caused by inconsistent data quality, and also alleviates the phase-processing flaws induced by unstable denoising and enhancement performance in single-input schemes.

2.1.3. Median-Unsharp Sharpening Enhancement (MUSE)

To enhance the robustness of subsequent cross-correlation registration and coherent summation, this paper introduces an image enhancement pipeline at the initial stage of the algorithm, constructing a MUSE and designing a supporting Adaptive Enhancement Factor Feedback Unit to realize closed-loop optimization of basic enhancement plus dynamic parameter tuning, so as to meet the requirements of speckle image reconstruction under complex illumination and noise interference.

Traditional image enhancement methods have obvious limitations: although histogram equalization improves overall contrast, it amplifies background noise, suppresses high-frequency effective signals, and tends to introduce artifacts in noisy regions [17]; cartoon-texture enhancement algorithms preserve details and suppress noise, but unnatural transitions may occur during fusion, and improper parameter settings will exacerbate distortion [18]; MF exhibits strong robustness against impulse noise and salt-and-pepper noise while preserving edges, but its ability to suppress continuous Gaussian noise is relatively limited [19,20]; USM enhances details by sharpening high-frequency components of images, yet it amplifies noise and requires additional noise suppression mechanisms [21]. Based on the comparative analysis of the above methods, this paper couples MF with mild USM and encapsulates them into a MUSE framework: first, MF is used to mitigate noise interference to compensate for the noise-amplification effect of USM, and then efficient detail enhancement is achieved through the integrated mild USM. Experimental results confirm that the sequence of MF followed by USM sharpening yields superior speckle reconstruction performance.

The formula for MF is as follows:

$$M(i,j) = \text{median}\{I(i+u, j+v) \mid u, v \in \{-1, 0, 1\}\} \tag{6}$$

where $M(i,j)$ is the median-filtered image at (i,j), median$\{\cdot\}$ is the median operator, $I(i+u, j+v)$ is the input pixel intensity, and $u, v \in \{-1, 0, 1\}$ specifies the 3×3 window.

The formula for USM is as follows:

$$f_{\text{out}}(x,y) = f(x,y) + \lambda \times HP[f(x,y)] \tag{7}$$

where $HP[.]$ denotes the high-pass filtering operation, and λ is the sharpening strength parameter.

To balance the enhancement effect and image details, our method performs linear fusion of the original image and the enhanced image, facilitating parameter adjustment and effect comparison in experiments:

$$I_{\text{fused}} = \alpha \cdot I_{\text{original}} + (1-\alpha) \cdot I_{\text{enhanced}} \tag{8}$$

where α in the formula is the linear enhancement parameter. Subsequently, the enhanced image is normalized to suppress extreme values and stabilize the input dynamic range, which is beneficial for subsequent registration and coherent summation:

$$I(i,j) = \left(\frac{A(i,j) - \min(A)}{\max(A) - \min(A)} \right) \times \max(Speckle) \tag{9}$$

where A represents the enhanced image before normalization, and $\max(Speckle)$ denotes the maximum grayscale value of the original speckle image.

Traditional MF and USM rely on fixed parameters, making it difficult to achieve a dynamic balance between noise suppression and detail enhancement under complex illumination conditions. To address this, this paper designs an Adaptive Enhancement

Factor Feedback Unit, which takes real-time features of speckle images as input and dynamically adjusts the key parameters of MF and USM through a closed-loop feedback mechanism, realizing adaptive optimization without manual intervention. The parameter adjustment of the feedback unit is based on three core features of speckle images: real-time signal-to-noise ratio (SNR_t), mean edge gradient (G_t), and noise ratio (η_t). Among them, SNR_t is used to characterize the overall noise interference degree of the image, calculated as:

$$\mathrm{SNR}_t = 10\log_{10}\left(\frac{I_S}{I_N}\right) \tag{10}$$

where I_S denotes the effective signal intensity of the speckle image captured under dark-room conditions and I_N is the average intensity of the pure background noise acquired with the laser emitter turned off. A lower SNR_t indicates stronger noise interference, requiring a corresponding increase in MF strength. The mean edge gradient (G_t) reflects the clarity of image edges, calculated using the Sobel operator with Equation (11):

$$G_t = \frac{1}{M \times N}\sum_{x=1}^{M}\sum_{y=1}^{N}\sqrt{G_x(x,y)^2 + G_y(x,y)^2} \tag{11}$$

where $G_x(x,y)$ and $G_y(x,y)$ are the gradient values of the pixel (x,y) in the x and y directions, respectively, and $M \times N$ is the pixel size of the speckle image. A smaller G_t means blunter edges, requiring an increase in USM sharpening strength. The noise ratio (η_t) is used to quantify the proportion of salt-and-pepper noise and random noise in the image, calculated by Equation (12):

$$\eta_t = \frac{\sum_{x=1}^{M}\sum_{y=1}^{N}\mathbb{I}\left(\frac{\left|I(x,y) - \bar{I}_{3\times3}(x,y)\right|}{\bar{I}_{3\times3}(x,y)} > T\right)}{M \times N} \tag{12}$$

where $\bar{I}_{3\times3}(x,y)$ is the mean of the 3×3 neighborhood centered at (x,y), T is the noise judgment threshold, and $\mathbb{I}(\cdot)$ is the indicator function. A higher η_t indicates a larger noise proportion, requiring a larger MF window.

Based on the extracted real-time features, the feedback unit dynamically adjusts the key parameters of MF and USM. For the MF window, to balance noise suppression and edge preservation effects, the window size needs to be adjusted dynamically with Equation (13):

$$W_t = \left\lfloor W_0 + k_1 \cdot \frac{\eta_t}{\eta_{max}} - k_2 \cdot \frac{G_t}{G_{max}} \right\rfloor \tag{13}$$

where W_0 is the basic filtering window, k_1, k_2 are adjustment coefficients, η_{max} and G_{max} are the normalized maximum values of noise ratio and edge gradient, and $\lfloor\cdot\rfloor$ is the floor function. The updated MF formula with the dynamic window is:

$$I_{mf}(x,y) = \mathrm{med}\{I(x+i, y+j) | (i,j) \in W_t\} \tag{14}$$

where $I_{mf}(x,y)$ denotes the median-filtered speckle image at pixel (i,j), $\mathrm{med}\{\cdot\}$ represents the median operation over the local window W_t, $I(x+i, y+j)$ is the intensity of the pixel at $(x+i, y+j)$, and W_t is the dynamically adjusted filtering window defined in the previous equation.

For the USM sharpening strength, dynamic adjustment is required by combining SNR and edge gradient with Equation (15):

$$\kappa_t = \kappa_0 \cdot \exp\left(a \cdot \frac{\mathrm{SNR}_t}{\mathrm{SNR}_{max}}\right) \cdot \exp\left(b \cdot \frac{G_{min}}{G_t}\right) \tag{15}$$

where κ_0 is the basic sharpening strength, a and b are adjustment coefficients, SNR_{max} is the normalized maximum SNR, and G_{min} is the minimum edge gradient. The updated USM formula with dynamic sharpening strength is:

$$I_{usm} = I + \kappa_t \cdot (I - I_{blur}) \tag{16}$$

where I is the input speckle image, κ_t is the dynamic sharpening strength determined by Equation (15), and I_{blur} is the Gaussian-blurred version of the input image I.

To ensure smooth transition of parameters between adjacent image frames or regions and avoid sudden changes in enhancement effects, an inertia term is introduced in the parameter adjustment process to construct a feedback iteration mechanism, with Equation (17):

$$\begin{cases} W_{t+1} = \lambda \cdot W_t + (1-\lambda) \cdot W_t^* \\ \kappa_{t+1} = \lambda \cdot \kappa_t + (1-\lambda) \cdot \kappa_t^* \end{cases} \tag{17}$$

where W_t^* and κ_t^* are the theoretical parameter values, and λ is the inertia coefficient. This mechanism ensures continuous changes in enhancement parameters and avoids artifacts caused by abrupt parameter jumps.

2.1.4. Phase-Aligned Coherent Summation (PACS)

After CSPO preprocessing and MUSE adaptive enhancement, the clutter noise and uneven illumination in speckle images are effectively suppressed, providing high-quality input data for subsequent phase reconstruction. However, a critical challenge exists in large-field-of-view scattering imaging: when the original speckle pattern is divided into multiple overlapping sub-blocks, lateral translation deviations inevitably occur among individual sub-speckles due to the randomness of scattering transmission. Direct coherent superposition of misaligned sub-blocks leads to phase cancellation, which severely degrades reconstruction quality and signal-to-noise ratio. To address this issue, this paper proposes the Phase Signed Coherent Summit (PACS) algorithm. Through cross-correlation displacement estimation, cyclic boundary alignment, coherent phase fusion, and closed-loop iterative optimization, the proposed method achieves accurate correction of phase mismatch among sub-blocks.

Before introducing this algorithm, we first present the pseudocode of PACS [see Algorithm 1].

The PACS algorithm first adopts a cross-correlation operation to quantitatively calculate the relative displacement between each sub-speckle [22] and the current reference image, and the mathematical formula is expressed as:

$$C_i = \mathcal{F}^{-1}\{\mathcal{F}(B_i) \odot \mathcal{F}(R)^*\} \tag{18}$$

where $\mathcal{F}$ and $\mathcal{F}^{-1}$ denote the two-dimensional Fourier transform and inverse Fourier transform, respectively. The superscript * represents the complex conjugate operation, and $\odot$ denotes the Hadamard product. The translation offset $(\Delta x_i, \Delta y_i)$ of the *i-th* sub-block can be determined by extracting the peak coordinates of the correlation coefficient matrix. To eliminate boundary truncation artifacts caused by conventional cropping-based alignment, the cyclic shift strategy is adopted in this work for sub-block registration:

$$B_i^{\text{align}} = \text{circshift}(B_i, [\Delta x_i, \Delta y_i]) \tag{19}$$

where B_i is the *i-th* sub-speckle, $[\Delta x_i, \Delta y_i]$ represent the horizontal and vertical displacement, and $\text{circshift}(\cdot)$ denotes the cyclic shift operation for sub-block registration. This

operation maintains a continuous phase distribution at the edges of sub-blocks, eliminates stitching artifacts, and ensures the effectiveness of subsequent coherent superposition.

After global alignment, all sub-speckles are unified to the same phase reference. Following alignment, a stable phase difference is formed between sub-blocks, so that the effective phase components can be enhanced through superposition, while random noise cancels each other out due to phase randomness, achieving signal enhancement and noise suppression. The mathematical expression for the coherent superposition of aligned sub-blocks is:

$$\phi = \frac{1}{N}\sum_{i=1}^{N} B_i^{\text{align}} \tag{20}$$

where N is the total number of sub-speckle blocks, and ϕ is the fused global phase distribution.

Based on Parseval's theorem of Fourier energy conservation [23], this paper calculates the average power spectrum of all sub-blocks to construct a fixed frequency-domain amplitude constraint throughout the iteration:

$$A = \sqrt{\left|\mathcal{F}\left(\mathcal{F}^{-1}(\overline{P})\right)\right|},\ \overline{P} = \frac{1}{N}\sum_{i=1}^{N}|\mathcal{F}(B_i)|^2 \tag{21}$$

where the fixed amplitude A remains constant throughout the iteration process, providing a stable physical prior constraint for complex signal reconstruction.

To continuously correct residual phase errors, this paper introduces an image iterative loop reconstruction mechanism, whose complete flow is shown in Algorithm 1. Before the iteration starts, one sub-speckle is randomly selected as the initial reference image R_0. Let the total number of iterations be K; in the k-th iteration, sub-block alignment and phase fusion are repeatedly performed based on the output result R_{k-1} of the $(k-1)$-th iteration. Then, the frequency-domain complex signal is synthesized by combining the fixed amplitude to complete the spatial-domain reconstruction:

$$I^{(k)} = \left|\mathcal{F}^{-1}\left\{A \odot \exp\left(j \cdot \angle\mathcal{F}\left(\phi^{(k)}\right)\right)\right\}\right| \tag{22}$$

The reconstructed image $I^{(k)}$ in this round is directly used as the new reference R_k for the next iteration after center correction, thus constructing a closed-loop dynamic update logic. The iteration termination condition is that the difference between the reconstructed results of two consecutive rounds is less than the preset threshold ε:

$$\text{diff} = \|I_k - R_{k-1}\|_2 < \varepsilon \tag{23}$$

If the termination condition is not met, the central region of $I^{(k)}$ is extracted as the new reference R_k for the next iteration, as expressed in Equation (24):

$$R_k = \text{center}(I^{(k)}) \tag{24}$$

As the iteration progresses, the phase deviation caused by sub-block misalignment is continuously compensated, and the phase solution gradually converges to the optimal steady-state solution.

After the iteration converges, the optimal phase distribution is coupled with the fixed amplitude to generate the final reconstruction result. Different from traditional phase retrieval algorithms with fixed references, PACS effectively solves the phase decoherence problem caused by speckle block processing through the cooperative mechanism of random initial reference, dynamic iterative update, and phase coherent superposition. Cyclic shift alignment ensures global phase continuity, and iterative optimization further sup-

presses residual noise and distortion, enabling the proposed algorithm to achieve higher reconstruction accuracy and robustness in complex scattering scenarios.

2.2. Experimental Setting

The optical system related to narrowband darkroom and non-darkroom equipment is shown in Figure 4a. The light emitted by a He-Ne laser (Daheng, Model DH-HN 250, Beijing, China, wavelength 632.8 nm) is expanded by a beam expander (BE) and then irradiated onto a rotating diffuser (RD) to generate pseudothermal light [24]. The light passes through iris 1 and illuminates objects with both length and width within 0.6 mm. In the experiment, frosted glass (Thorlabs, Model DG 10-220, 220 grit, Newton, NJ, USA) was selected as the scattering medium and placed 450 mm away from the object. The scattered object light passes through the iris (i.e., iris 2) placed 10 mm away from the scattering medium, and after passing through a filter (Hengyang, central wavelength (CWL) 632.8 nm, Hunan, China), it is captured by a CMOS camera (MindVision, Model MV-SUA 230 GM, Shenzhen, China) resolution 1920 × 1200 pixels, pixel size: 5.86 μm/pixel) with an exposure time of 0.5 s. Among them, the diameter of iris 1 is 5 mm, and the diameter of iris 2 is 3 mm. Appropriate iris size is crucial for speckle and autocorrelation quality and can also moderately reduce noise interference caused by stray light [25]. All reconstruction processes were carried out on a PC equipped with a Ryzen 5 5600 CPU and 16 GB DDR4 RAM.

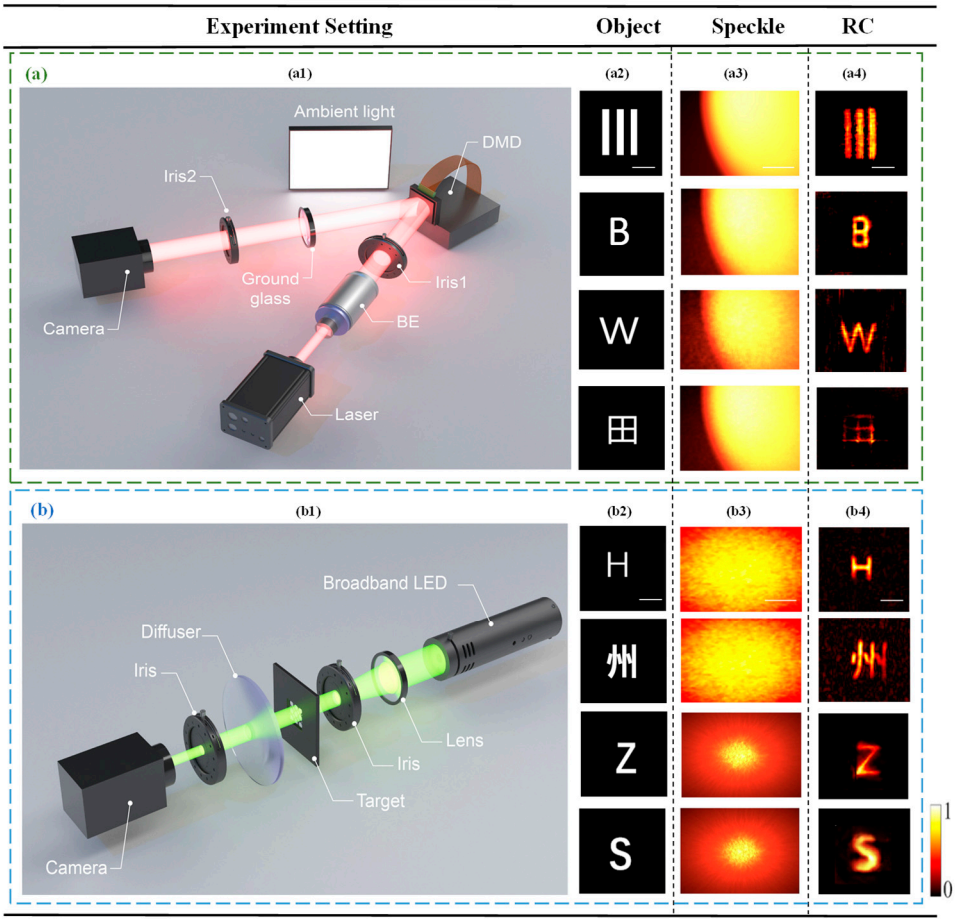


Figure 4. Schematic of the optical system. (**a**) The optical system and reconstruction results under narrowband lighting. (**a1**) Narrowband lighting imaging equipment. (**a2**) Object image under narrowband lighting. (**a3**) Corresponding speckle. (**a4**) Reconstruction of (**a3**). (**b**) The optical system and reconstruction results under broadband lighting. (**b1**) Broadband lighting imaging equipment. (**b2**) Object image under broadband lighting. (**b3**) Corresponding speckle. (**b4**) Reconstruction of (**b3**). Scale bars: 703.20 μm in (**a3**,**b3**), 281.28 μm in others.

The design for capturing broadband speckle images is illustrated in Figure 4b. Broadband light for the system is supplied by a white light LED (Thorlabs, model MBB1L3, Newton, NJ, USA), which has a wavelength range of 400–1100 nm and a bandwidth of 280 nm. This light first illuminates the target (a metal mask with length and width both within 0.6 mm), then travels through a diffuser, and is ultimately captured by the camera. The object distance and image distance of the setup are configured to 30 cm and 6 cm, respectively. Notably, in this study, aside from the open-source speckle data referenced earlier, the broadband speckle images discussed in Section 3.3 were acquired using the imaging system shown in Figure 4b.

The intensity of ambient light is regulated by adjusting the brightness of the light panel, and it is quantified using the SNR [26]. In our study, SNR is defined as the same as in Equation (10). In addition, peak signal-to-noise ratio (PSNR) is introduced to quantitatively evaluate the reconstruction quality of obtained images [27], which is calculated based on the mean square error (MSE) between the ground-truth image and the reconstructed image, and its specific calculation formula is defined as Equation (25):

$$PSNR = 10 \log_{10} \left(\frac{(2^n - 1)^2}{\text{MSE}} \right) \tag{25}$$

Furthermore, the Structural Similarity Index (SSIM) [28] is adopted to comprehensively assess the structural fidelity and perceptual quality of the reconstructed images. It evaluates the similarity between the ground truth and the reconstruction by jointly considering luminance, contrast, and structural information, defined as Equation (26):

$$\text{SSIM}(x, y) = \frac{(2\mu_x\mu_y + C_1)(2\sigma_{xy} + C_2)}{(\mu_x^2 + \mu_y^2 + C_1)(\sigma_x^2 + \sigma_y^2 + C_2)} \tag{26}$$

where in μ_x and μ_y denote the mean intensities, σ_x and σ_y denote the standard deviations, and σ_{xy} denotes the cross-covariance of the two images, while C_1 and C_2 are small constants introduced to avoid division by zero.

Through experiments, the Gaussian kernels employed for illumination elimination are configured such that the large Gaussian kernel is set to 31×31 and the small Gaussian kernel to 5×5 [29]. In Equation (12), the noise judgment threshold T is calibrated to 0.2, and the indicator function $\mathbb{I}(\cdot)$ takes a value of 1 if the condition inside the parentheses is satisfied, and 0 otherwise. In Equation (13), the basic filtering window W_0 is set to 3, the adjustment coefficients k_1 and k_2 are set to 4 and 2, respectively, and the normalized maximum values of the noise ratio η_{max} and edge gradient G_{max} are both set to 1. The window size is constrained to $3 \leq W_t \leq 7$ (odd numbers are used to prevent pixel offset, thereby avoiding over-blurring or insufficient filtering). In Equation (15), the basic sharpening strength κ_0 is set to 0.5, the adjustment coefficients a and b are calibrated to 0.8 and 0.6, respectively, the normalized maximum SNR SNR_{max} is set to 1, and the minimum edge gradient G_{min} is calibrated to 5 to avoid a denominator of zero. To prevent noise amplification or insufficient sharpening, the sharpening strength is constrained to $0.1 \leq \kappa_t \leq 1.2$ [30]. In Equation (17), the inertia coefficient λ is set to 0.7. In Equation (23), the preset threshold ε is set to 10^{-3}. In terms of the number of iterations, the process will converge when the number of iterations is set to about 20.

3. Results

3.1. The Effectiveness of the Dual-Input Algorithm

We first compare PACS with the conventional Coherent accumulation (CA) method [31], then verify the necessity of the dual-input strategy by comparing the reconstruction results using only a single input with those using the dual input, as shown in Figure 5.

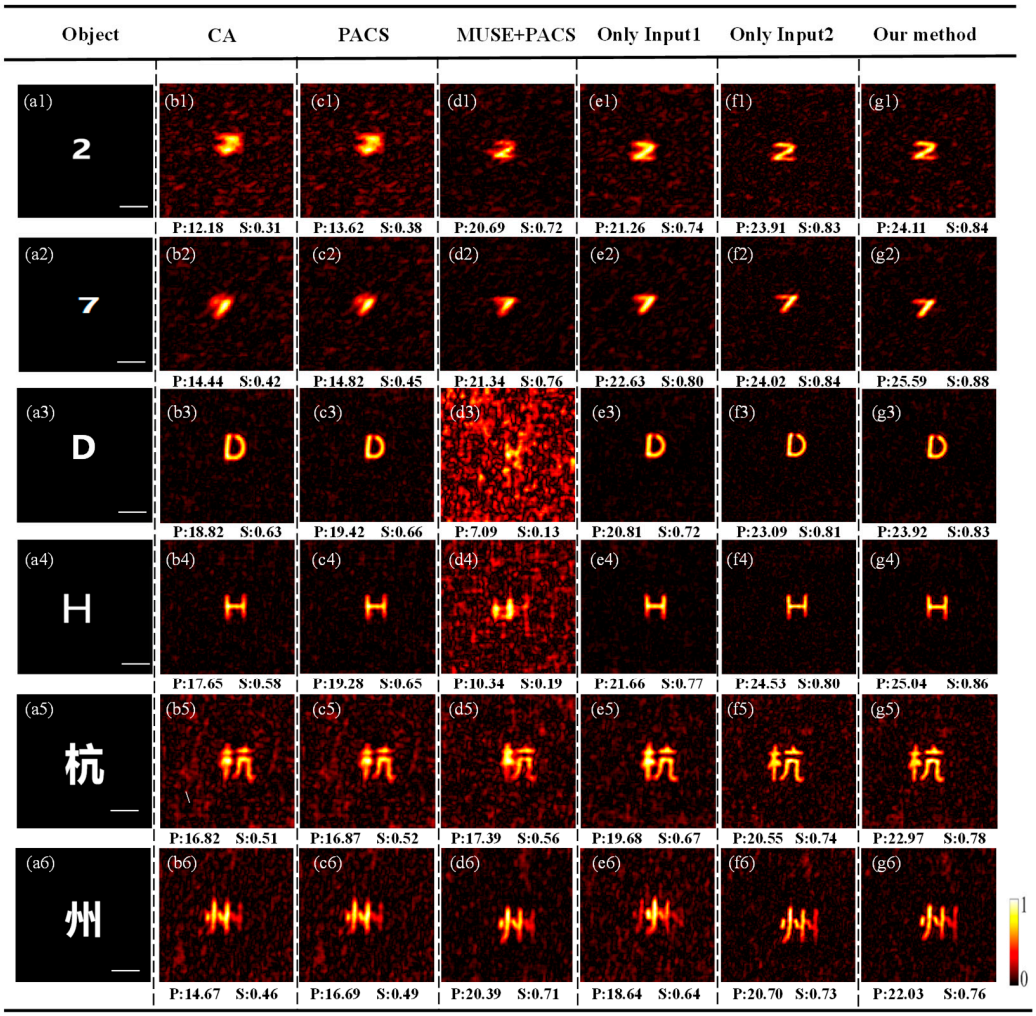


Figure 5. Reconstruction results from experiments with different input ports. (**a1**–**a6**) Object image. (**b1**–**b6**) Reconstruction results of the phase algorithm CA. (**c1**–**c6**) Reconstruction results of the phase algorithm PACS. (**d1**–**d6**) Reconstruction results with MUSE + PACS. (**e1**–**e6**) Reconstruction results only by input1. (**f1**–**f6**) Reconstruction results only by input2. (**g1**–**g6**) Reconstruction results with our method. For each reconstructed image, the quantitative metrics P (PSNR, in dB) and S (SSIM) are provided below. Scale bar: 281.28 μm.

From the perspectives of both PSNR and visual effects, the proposed method demonstrates significant advantages over all comparative schemes. The baseline CA method [see Figure 5(b1–b6)] generally produces reconstructed images with blurred edges, lost details, and low contrast. In particular, for complex Chinese character targets such as "Hang" [see Figure 5(b5)] and "Zhou" [see Figure 5(b6)], the contours and stroke details are barely distinguishable, and their PSNR values are the lowest among all methods. This indicates that the traditional CA method has obvious limitations in handling non-stationary noise and multi-scale speckle characteristics. After introducing PACS on the basis of CA, the reconstruction effect is initially improved [32]. PACS can suppress noise at different scales and enhance the edges of targets, making the contours of simple targets such as "2", "7", and "D" [see Figure 5(c1–c3)] clearer, and the PSNR values are also improved to a certain extent. However, for complex structural targets such as "Hang" and "Zhou" [see Figure 5(c5,c6)], PACS still struggles to fully restore details, and noise residues remain in some scenarios, indicating that a single multi-scale decomposition module is insufficient to handle complex speckle reconstruction tasks.

With the further introduction of MUSE, the PSNR values of some targets are improved, but obvious performance degradation occurs for targets such as "D" [see Figure 5(d3)] and "H" [see Figure 5(d4)], with PSNR values even lower than the baseline CA method. This reveals the inherent defects of a single enhancement module: although MUSE can improve details in certain scenarios, it also amplifies background noise and introduces severe artifacts, leading to unstable reconstruction results that are difficult to adapt to different types of targets and noise conditions.

The results of using only a single input intuitively reveal the necessity of the dual-input strategy. Whether relying solely on Input1 or Input2, the reconstruction effect is significantly inferior to the complete dual-input method, and the performance fluctuates considerably under different inputs. For example, on the "D" [see Figure 5(e3,f3)] and "H" targets [see Figure 5(e4,f4)], the PSNR of only Input2 is significantly higher than that of only Input1, while on the "Hang" [see Figure 5(e5,f5)] and "Zhou" targets [see Figure 5(e6,f6)], the performance of the two is relatively close. This indicates that a single input cannot fully utilize the complementary information under different illumination conditions, making it difficult to balance noise suppression and detail preservation.

In contrast, our method achieves the highest PSNR values on all targets, with the most outstanding visual effects. The reconstructed images feature clear target contours, rich details, and thorough noise suppression. Whether for simple numbers or complex Chinese characters, the morphology and texture of the original targets can be highly restored [see Figure 5(g1–g6)]. This benefits from the effective fusion of different illumination information by the dual-input strategy and the synergistic effect of PACS and MUSE, enabling the entire framework to achieve comprehensive improvements in noise suppression, detail preservation, and robustness.

3.2. Analysis of Low-Quality Speckle Under Narrowband Lighting

In the previous set of experiments, we demonstrated the effectiveness of our method. Next, we focus on low-quality speckles affected by ambient light. We applied it to non-darkroom conditions to verify the reliability of the enhancement method, with quality measured by SNR. The three sets of experiments were set to SNR = 3.89 dB, 1.93 dB, and −1.78 dB, respectively, as shown in Figure 6.

We selected three common enhancement methods (HE, MF, and USM), which were mentioned in the previous section, and conducted ablation experiments for comparison. From the perspectives of reconstructed images and autocorrelation images, the HE method [33,34] achieves acceptable restoration quality when the SNR is relatively high, but its restoration quality is poor for extremely low-quality speckles. This reason can be attributed to the sensitivity of HE [35] to the fusion factor. MF [36–38] shows significant improvements compared to HE, but the images it restores contain more noise. Although USM exhibits increased brightness compared to the previous two methods, it also reveals the issue of unclear edges in USM. HE + MF indeed incorporates the advantages of both methods, but it also introduces artifacts caused by over-enhancement [see Figure 6f] [39]. HE + USM solves the problem of unclear speckle edges to a certain extent, but the effect is clearly insufficient [see Figure 6g]. The MF + USM method combines the two methods of MF and USM without causing over-enhancement. Even at SNR = −1.78 dB, it still achieves excellent restoration results [see Figure 6h]. This fusion enhancement algorithm demonstrates excellent applicability.

To compare the effectiveness of this enhancement method, we compare it with several common low-quality speckle restoration methods currently available. Additionally, to highlight the superiority of our method, we utilize low-quality speckles with negative SNR values for experimental comparison as shown in Figure 7.

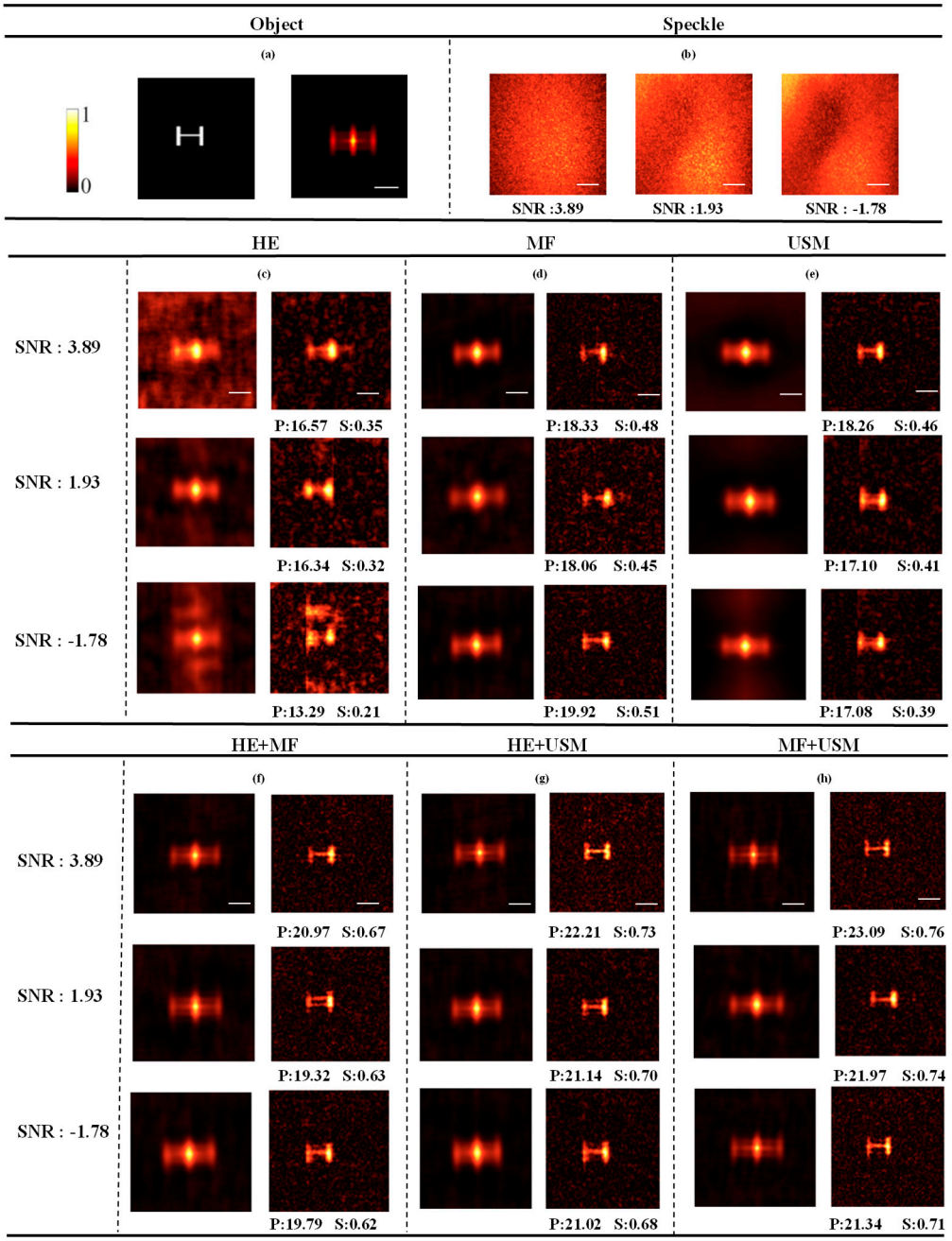


Figure 6. Speckle restoration performance of different enhancement methods. (**a**) Object image captured by the CMOS. (**b**) Object speckle of (**a**). (**c**) Speckle and autocorrelation images restored by the HE method. (**d**) Speckle and autocorrelation images restored by the MF method. (**e**) Speckle and autocorrelation images restored by the USM method. (**f**) Speckle and autocorrelation images restored by the HE + MF method. (**g**) Speckle and autocorrelation images restored by the HE + USM method. (**h**) Speckle and autocorrelation images restored by the MF + USM method. For each reconstructed image, the quantitative metrics P (PSNR, in dB) and S (SSIM) are provided below. Scale bar: 281.28 μm.

In Figure 7, we used low-quality speckles for the test. SCHF is an adaptive homomorphic filtering method that achieved good results in non-darkroom and wide-band light scenarios [39]. In our experiment, SCHF also showed good performance [see Figure 7d]. However, it produced more artifacts and noise in digital images. NRSI is a dual-spectrum enhancement method that was applied to low-quality enhancement algorithms [40]. Although its performance is superior to that of SCHF, there is still room for improvement in

terms of restored brightness and edge clarity [see Figure 7e]. Our method [see Figure 7f] eliminates more artifacts present in the above two methods and effectively enhances brightness, whether in simple or complex images.

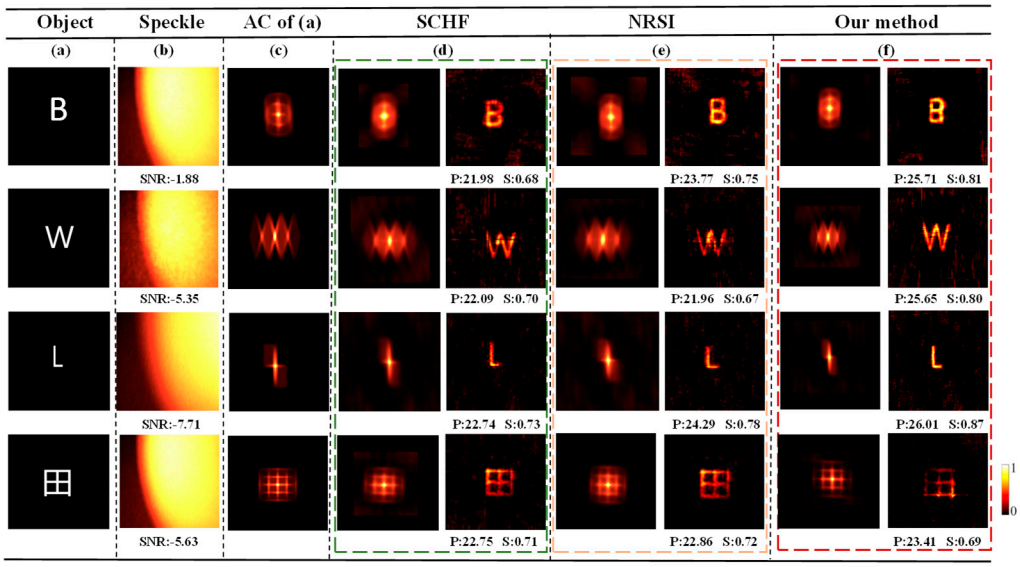


Figure 7. Experimental comparison with existing enhancement algorithms for low-quality speckle restoration. (**a**) Object image captured by the CMOS. (**b**) Object speckle of (**a**). (**c**) Autocorrelation images of (**a**). (**d**) Speckle and autocorrelation images restored by the SCHF method. (**e**) Speckle and autocorrelation images restored by the NRSI method. (**f**) Speckle and autocorrelation images restored by our method. For each reconstructed image, the quantitative metrics P (PSNR, in dB) and S (SSIM) are provided below. Scale bar: 281.28 μm.

Since we have improved the phase retrieval algorithm, it is necessary for us to select several common algorithms to demonstrate the effectiveness of this improvement. In Figure 8, we conducted experiments using speckles of varying quality obtained from the same target.

A comparative analysis of the reconstruction performance of the HIO, CA, and PACS algorithms was conducted on the low-quality speckle data [41,42]. The results indicate that the HIO [41] algorithm exhibits considerable limitations, as its reconstruction is dominated by significant, non-removable noise. The CA algorithm [42], serving as a baseline for comparison, demonstrates a marked improvement over HIO, with a substantial reduction in noise. However, residual artifacts, particularly at the edges, persist and manifest as severe structural adhesion between features under extremely low SNR conditions [see Figure 8c]. Physically, this is because conventional methods such as HIO and CA rely on fixed reference blocks and static prior constraints, making them unable to adaptively correct the phase incoherence and noise interference caused by complex scattering and ambient light. In contrast, the PACS algorithm, which is an improvement derived from the CA framework, effectively mitigates this issue of structural adhesion, yielding superior reconstruction quality with minimal artifacts.

To demonstrate the effectiveness of this phase retrieval algorithm, we conduct experiments by selecting lower quality speckles and targets with more complex structures, as shown in Figure 9. This further verifies that the dynamic reference and phase alignment mechanism in PACS can effectively handle the phase inconsistency caused by severe scattering and noise, thus maintaining stable reconstruction performance even under extremely low-SNR conditions.

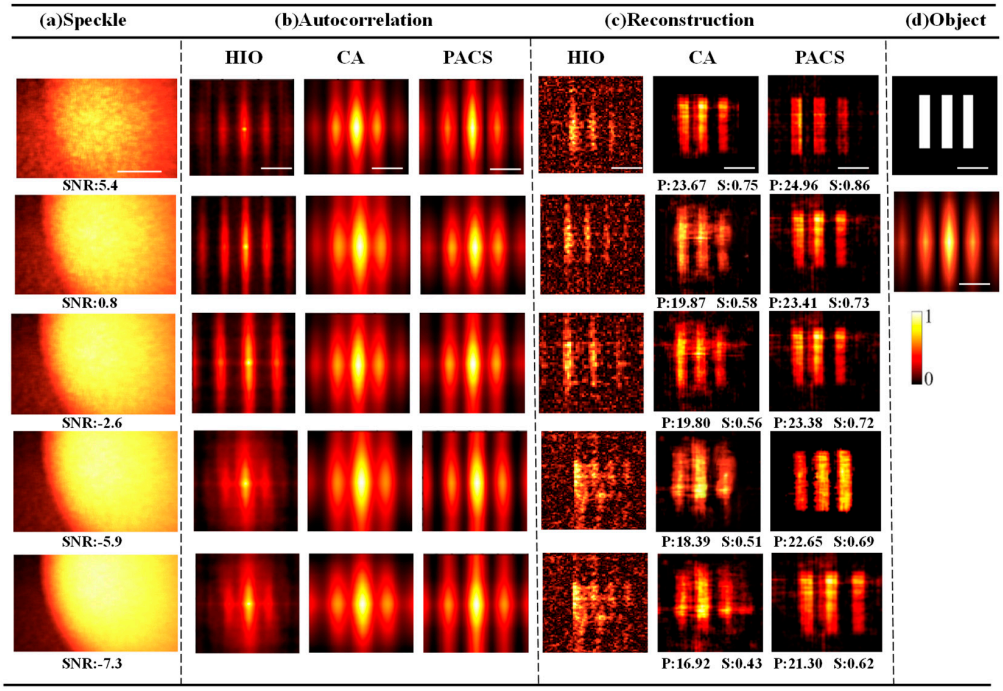


Figure 8. Comparison with common phase retrieval algorithms. (**a**) Original low-quality speckle image. (**b**) Autocorrelation images of (**a**). (**c**) Speckle images restored by the three different methods. (**d**) Object image captured by the CMOS. For each reconstructed image, the quantitative metrics P (PSNR, in dB) and S (SSIM) are provided below. Scale bars: 703.20 μm in (**a**), 281.28 μm in others.

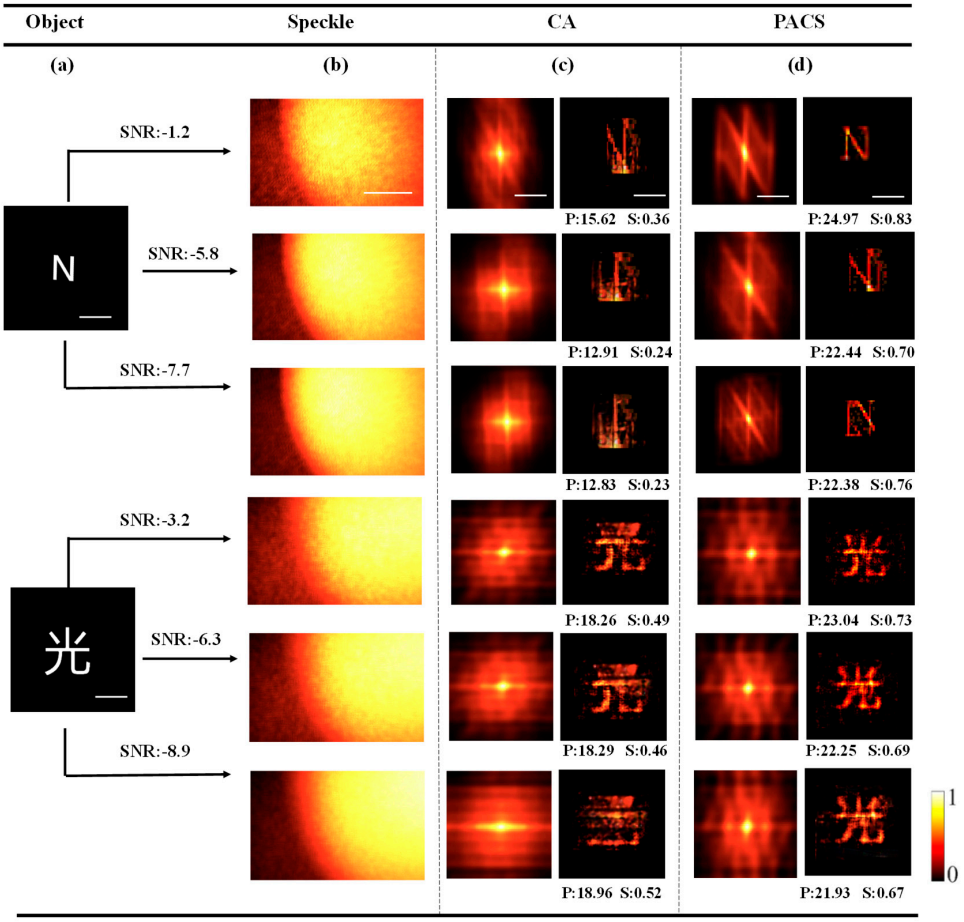


Figure 9. Experiments on the recovery performance of targets with more complex structures. (**a**) Object image captured by the CMOS. (**b**) Object speckle of (**a**). (**c**) Speckle and autocorrelation images

restored by the CA. (**d**) Speckle and autocorrelation images restored by the PACS. For each reconstructed image, the quantitative metrics P (PSNR, in dB) and S (SSIM) are provided below. Scale bars: 703.20 μm in (**b**), 281.28 μm in others.

When comparing more complex images including letters and Chinese characters [see Figure 9a], the CA phase retrieval algorithm exhibits more significant issues. When the SNR is below −5 dB, the CA algorithm can barely even resolve the image to be recovered [see Figure 9c]. In contrast, although the PACS algorithm exhibits some artifacts when the SNR is extremely low, its image recovery quality is still significantly superior to that of CA [see Figure 9d].

3.3. Analysis of Lower-Quality Speckle Under Broadband Lighting

In the previous experiments, we discussed not only the reliability of our method under darkroom conditions but also the recovery performance of this method in the presence of low-quality speckles and strong ambient light interference. However, all these scenarios involve narrowband light. In this chapter, we will focus on discussing the role of this method in wide-band light.

Under broadband illumination, we captured the corresponding speckle images. We first investigate the reconstruction performance under a 280 nm bandwidth, as shown in Figure 10.

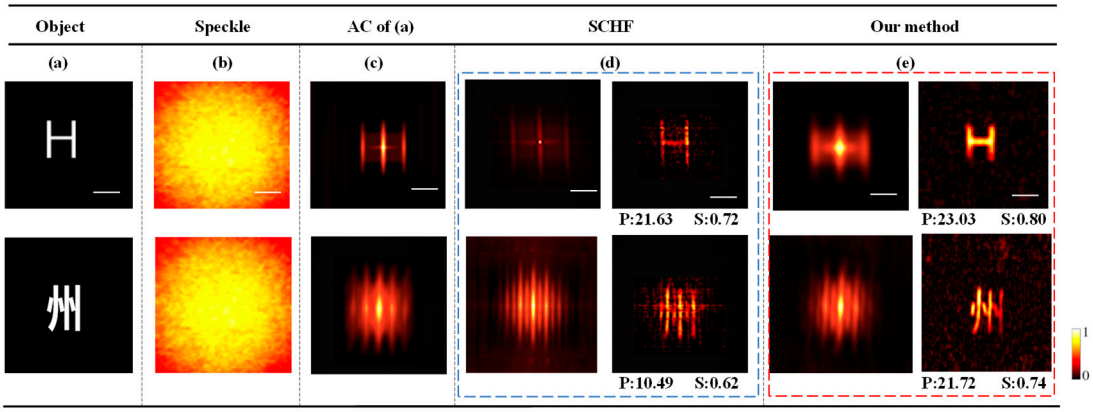


Figure 10. Recovery performance with a 280 nm spectral bandwidth. (**a**) Object image captured by the CMOS. (**b**) Object speckle of (**a**). (**c**) Speckle and autocorrelation images of (**a**). (**d**) Speckle and autocorrelation images restored by SCHF. (**e**) Speckle and autocorrelation images restored by our method. For each reconstructed image, the quantitative metrics P (PSNR, in dB) and S (SSIM) are provided below. Scale bar: 281.28 μm.

Liu et al. proposed the SCHF method for broadband light, which significantly improved the effect of broadband light image restoration [39]. Therefore, we compare our method with SCHF. SCHF has certain limitations: although its adaptive homomorphic filtering approach can automatically control parameters, broadband light speckles are very sensitive to the enhancement coefficient. Moreover, SCHF cannot guarantee that the minimum EP value corresponds exactly to the highest PSNR, making this parameter auto-determination method not accurate enough. This inaccuracy is also reflected in the fact that the speckles restored by SCHF contain many noise points in the concentrated area at the image center [see Figure 10d]. Our method relies on a fixed parameter ratio; while it requires manual setting of the enhancement coefficient, both its robustness and restoration effect are superior to those of SCHF [see Figure 10e].

Under broadband illumination, we captured the corresponding speckle images. We then set the spectral bandwidth to 200 nm and continued the experiment, as shown in Figure 11.

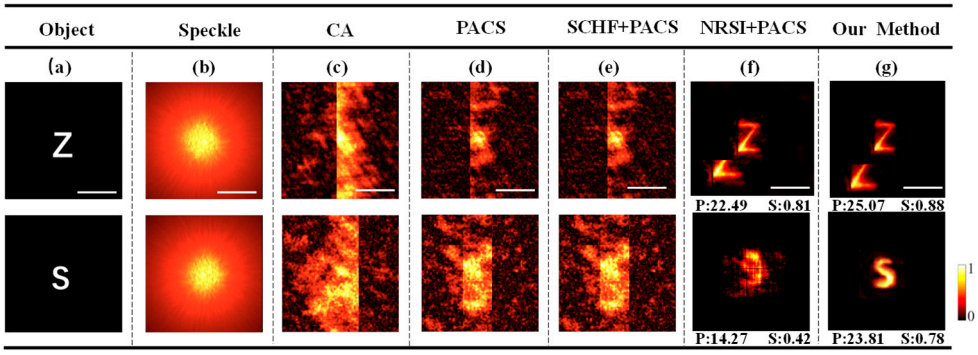


Figure 11. Recovery performance with a 200 nm spectral bandwidth. (**a**) Object image. (**b**) Object speckle of (**a**). (**c**) Speckle images restored by CA. (**d**) Speckle images restored by PACS. (**e**) Speckle images restored by SCHF + PACS. (**f**) Speckle images restored by NRSI + PACS. (**g**) Speckle images restored by our method. For each reconstructed image, the quantitative metrics P (PSNR, in dB) and S (SSIM) are provided below. Scale bar: 281.28 μm.

Liu et al. and Cui et al. have successively proposed methods for broadband recovery, and both achieved good results [39,40]; however, there is still room for improvement in terms of edge sharpness. In Figure 11, it can be seen that the PACS method is very suitable for broadband applications. Even without incorporating any enhancement algorithms, its speckle recovery quality far exceeds that of CA. The SCHF method has almost no effect on image quality enhancement [see Figure 11e]. The NRSI method has a significant improvement on PACS, but its recovery results still contain artifacts, leaving considerable room for improvement [see Figure 11f]. The method we proposed not only effectively enhances the performance of PACS but also solves the significant artifact problem [see Figure 11g].

In the reconstruction task of continuous broadband spectrum speckles, we compared our method with Guo's method [43], Wu's method [44], and the NRSI enhancement method. The results show that the proposed method not only effectively suppresses artifacts but also achieves the highest PSNR and SSIM values, demonstrating significant advantages and good applicability in continuous broadband scenarios, as shown in Figure 12.

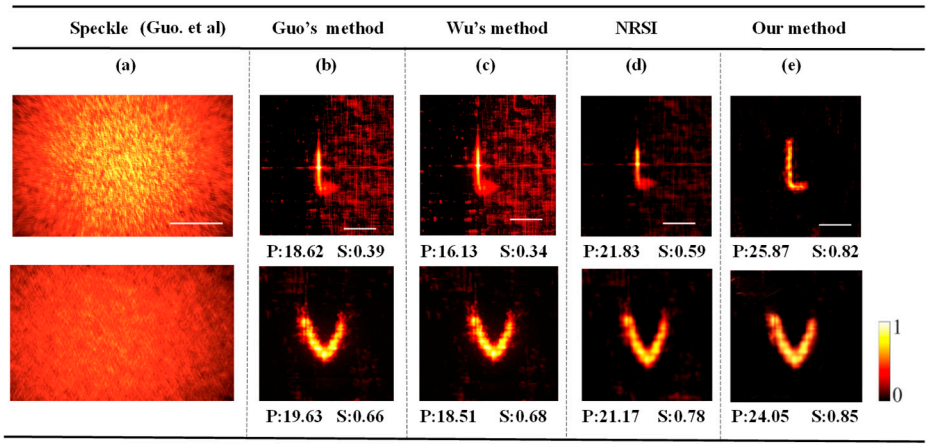


Figure 12. Recovery performance with a 100 nm spectral bandwidth under continuous spectrum illumination. (**a**) Original speckle image. (**b**) Reconstruction by Guo's method. (**c**) Reconstruction

by Wu's method. (**d**) Reconstruction by NRSI method. (**e**) Reconstruction by our method. For each reconstructed image, the quantitative metrics P (PSNR, in dB) and S (SSIM) are provided below. Scale bars: 703.20 μm in (**a**), 281.28 μm in others.

4. Discussion

4.1. Efficiency Analysis of the Proposed Algorithm

To evaluate the computational efficiency of our method, we compare its runtime with that of the state-of-the-art methods mentioned above, including SCHF, NRSI, and CA. The detailed comparison results are presented in Table 1.

Table 1. Efficiency comparison of the proposed method in different scenarios.

Different Lighting	CA	HIO	GS	Ours
Narrowband Lighting	18.91	19.20	16.23	29.47
Broadband Lighting	23.44	29.75	27.84	41.07

From the efficiency comparison in Table 1, we note that our method currently has a higher computational cost than the compared methods (CA, HIO, GS) under both narrowband and broadband lighting scenarios. This is mainly due to the additional preprocessing and optimization steps introduced in our pipeline, which increase runtime overhead while improving reconstruction performance.

4.2. Analysis of Real-Scene Recovery Performance Under Unknown Scattering Media

As mentioned earlier, the proposed algorithm exhibits strong practical application potential. To further validate the effectiveness and generalization ability of the proposed processing pipeline, we attempt to integrate the preprocessing module with existing dehazing algorithms and test the adaptability of the algorithm under heavy haze conditions, where haze acts as a typical strong scattering medium. Specifically, we embed the proposed pipeline into the classic edge-preserving smoothing algorithm, bilateral filtering, and conduct dehazing tests on real-world traffic scene images. The corresponding dehazing results are presented in Figure 13, where Figure 13a–d represent the recovery effects under different haze conditions ranging from light to heavy.



Figure 13. Qualitative comparison of recovery methods on real-world scene images. (**a**–**d**) show the recovery results for images with interference density increasing from light to heavy.

As shown in the top row of Figure 13, the original disturbed images suffer from severe visibility degradation, low contrast, and color desaturation, especially in heavy interference scenarios [see Figure 13d], where distant objects and markings are almost indistinguishable. After applying our recovery pipeline integrated with bilateral filtering, the restored images

in the bottom row exhibit significant visual improvements. The overall contrast and color saturation are effectively recovered, and the details of objects, pedestrians, and key signs are clearly enhanced, even in the most challenging heavy-interference conditions.

From a qualitative perspective, the proposed method demonstrates strong robustness to varying interference levels. In light interference scenarios [see Figure 13a], the recovery is natural and free of obvious artifacts. In medium interference [see Figure 13b,c], the method effectively removes interference while preserving fine details and edge information, which is crucial for scene analysis. Even in heavy interference [see Figure 13d], the method still achieves satisfactory recovery performance, significantly improving the visibility of distant objects without introducing noticeable color distortion or over-smoothing.

5. Conclusions

In this paper, we propose a unified speckle imaging framework to address the core challenge of poor reconstruction quality in SCI caused by ambient light interference, speckle noise, and phase incoherence. The framework innovatively constructs a dual-input synchronous transmission architecture, which effectively breaks through the limitations of traditional single-path reconstruction methods. After unified preprocessing by CSPO, dual-channel data are fed into the PACS in parallel to achieve efficient reconstruction and high-precision reconstruction, respectively, and the two types of reconstruction results are adaptively fused within PACS, enabling the framework to balance imaging efficiency and reconstruction quality under complex lighting conditions with ambient light interference. Meanwhile, an adaptive enhancement factor feedback mechanism is designed for MUSE, which dynamically adjusts the enhancement coefficients of MF and USM according to the real-time features of speckle images. This mechanism breaks the limitation of fixed parameters in traditional methods, realizes an adaptive balance between noise suppression and detail enhancement, and further improves the robustness of the system in extreme lighting environments. In addition, a dynamic reference update mechanism is introduced in PACS, where the reconstructed result after each iteration replaces the initial reference block. Combined with the fixed amplitude derived from multi-block power spectrum averaging, it realizes iterative optimization of phase accuracy, effectively suppresses random speckle noise, and improves the SNR of reconstructed images under complex scattering conditions.

The proposed framework adopts a modular and loosely coupled design with unified interfaces and independent logic among modules. It can be flexibly embedded into various recovery algorithms as a general speckle enhancement and reconstruction unit, significantly improving the restoration performance of low-quality speckle images under multi-light-source conditions with ambient light and effectively expanding the practical application scenarios of SCI technology. Experimental results demonstrate that the proposed method maintains excellent restoration performance even when the SNR of speckle images is as low as -8.7 dB under narrowband illumination with ambient light interference and broadband illumination with different bandwidths (100 nm, 200 nm, 280 nm), and it also achieves notable improvements in real-scene recovery under unknown scattering media. Nevertheless, the current framework involves additional preprocessing and iterative steps, resulting in higher computational overhead than conventional methods. Future work will focus on optimizing key modules and exploring lightweight implementations to further improve efficiency while preserving reconstruction quality.

Author Contributions: Conceptualization, A.L. and G.C.; Methodology, A.L., G.C., Y.C. and J.M.; Software, A.L. and W.C.; Validation, Y.C. and J.M.; Formal analysis, Z.L.; Investigation, L.F.; Resources, G.C. and J.Z.; Data curation, A.L. and W.C.; Writing—original draft, A.L.; Writing—review and editing, A.L. and G.C.; Visualization, L.F. and Z.L.; Supervision, G.C.; Project administration, G.C.

and J.Z.; Funding acquisition, G.C. and J.Z. All authors have read and agreed to the published version of the manuscript.

Funding: Natural Science Foundation of Zhejiang Province (Grant Nos. LMS26F050009 and LMS26F050010); Fundamental Research Funds for the Provincial Universities of Zhejiang (Grant No. GK249909299001-011).

Data Availability Statement: The original contributions presented in this study are included in the article. Further inquiries can be directed to the corresponding author.

Conflicts of Interest: The authors declare no conflicts of interest.

Abbreviations

The following abbreviations are used in this manuscript:

SCI	Speckle correlation imaging
DL	Deep learning
OME	Optical memory effect
OTF	Optical transfer function
SNR	Signal-to-noise ratio
GS	Gerchberg and Saxton
FT	Fourier transform
DCT	Discrete cosine transform
DWT	Discrete wavelet transform
CSPO	Correction-smoothing-phase optimization
MUSE	Median-unsharp sharpening enhancement
PACS	Phase-aligned coherent summation
PSF	Point spread function
MF	Median filtering
USM	Unsharp masking
BE	Beam expander
CWL	Central wavelength
PSNR	Peak signal-to-noise ratio
SSIM	Structural similarity index
MSE	Mean square error
CA	Coherent accumulation
SCHF	Liu's method
NRSI	Cui's method

References

1. Freund, I.; Rosenbluh, M.; Feng, S. Memory effects in propagation of optical waves through disordered media. *Phys. Rev. Lett.* **1988**, *61*, 2328–2331. [CrossRef]
2. Katz, O.; Heidmann, P.; Fink, M.; Gigan, S. Non-invasive single-shot imaging through scattering layers and around corners via speckle correlations. *Nat. Photonics* **2014**, *8*, 784–790. [CrossRef]
3. Yuan, Y.; Chen, H. Dynamic noninvasive imaging through turbid media under low signal-noise-ratio. *New J. Phys.* **2020**, *22*, 093046. [CrossRef]
4. Lu, D.; Xing, Q.; Liao, M.; Situ, G.; Peng, X.; He, W. Single-shot noninvasive imaging through scattering medium under white-light illumination. *Opt. Lett.* **2022**, *47*, 1754–1757. [CrossRef]
5. Li, W.; Xi, T.; He, S.; Liu, L.; Liu, J.; Liu, F.; Wang, B.; Wei, S.; Liang, W.; Fan, Z.; et al. Single-shot imaging through scattering media under strong ambient light interference. *Opt. Lett.* **2021**, *46*, 4538–4541. [CrossRef]
6. Miao, J.; Cai, F.; Qin, T.; Bai, L.; Guo, E.; Shi, Y.; Han, J. Adaptive windowing for photon-efficient non-line-of-sight imaging under high ambient light. *Opt. Express* **2025**, *33*, 44522–44542. [CrossRef]
7. Qiao, M.; Zhang, Y.; Yang, H.; Bai, L.; Dong, X.; Zhang, T.; Liu, J.; Liu, F.; Gigan, S.; Shao, X. Harnessing forward scattering effect for high dynamic imaging. *Photonix* **2025**, *6*, 41. [CrossRef]

8. Liu, J.; Luo, X.; Duan, J.; Feng, Y.; Xiang, M.; Dong, X.; Liu, J.; Liu, F.; Shao, X. Single-shot broadband scattering imaging based on speckle frequency refinement. *Chin. Opt. Lett.* **2026**, *24*, 011101. [CrossRef]
9. Tang, C.; Wang, F.; Tang, Z.; Chu, Y.; Situ, G. TransFNet: A physics-enhanced transformer for speckle correlation imaging. *Opt. Commun.* **2025**, *591*, 132126. [CrossRef]
10. Fienup, J.R. Phase retrieval algorithms: A comparison. *Appl. Opt.* **1982**, *21*, 2758–2769. [CrossRef] [PubMed]
11. Gerchberg, R.W.; Saxton, W.O. A practical algorithm for the determination of the phase from image and diffraction plane pictures. *Optik* **1972**, *35*, 237–246.
12. Candes, E.J.; Strohmer, T.; Voroninski, V. PhaseLift: Exact and stable signal recovery from magnitude measurements via convex programming. *Commun. Pure Appl. Math.* **2013**, *66*, 1241–1274. [CrossRef]
13. Yeh, C.; Tabrikian, J.; Lee, T. Coherent averaging technique: A tutorial review Part 1: Noise reduction and signal extraction and the equivalent filter. *IEEE Trans. Instrum. Meas.* **1986**, *35*, 275–280. [CrossRef]
14. Mao, Y.; Ding, Y.; Gu, S.; Sharma, K.P.; Gupta, D.N. A deep journey into image enhancement: A survey of current and emerging trends. *Signal Process. Image Commun.* **2023**, *114*, 116933. [CrossRef]
15. Wang, Y.; Um, M.; Zhang, J.H.; An, S.; Lyu, M.; Zhang, J.-N.; Duan, L.-M.; Yum, D.; Kim, K. Single-qubit quantum memory exceeding ten-minute coherence time. *Nat. Photonics* **2018**, *12*, 185. [CrossRef]
16. Wang, X.; Liu, Z.; Tang, S.; Wu, X. Laser speckle contrast imaging based on spatial frequency filtering. *Photonic Sens.* **2023**, *13*, 230–240. [CrossRef]
17. Onyedinma, E.; Onyenwe, I.; Inyiama, H. Performance evaluation of histogram equalization and fuzzy image enhancement techniques on low contrast images. *arXiv* **2019**, arXiv:1909.03957. [CrossRef]
18. Li, K.; Wen, Y.-W.; Chan, R.H. Cartoon–Texture Image Decomposition Using Least Squares and Low-Rank Regularization. *J. Math. Imaging Vis.* **2025**, *67*, 5. [CrossRef]
19. Hwang, H.; Haddad, R.A. Adaptive median filters: New algorithms and results. *IEEE Trans. Image Process.* **1995**, *4*, 499–502. [CrossRef]
20. Gonzalez, R.C.; Woods, R.E. *Digital Image Processing*, 4th ed.; Pearson: Boston, MA, USA, 2018.
21. Polesel, A.; Ramponi, G.; Mathews, V.J. Image enhancement via adaptive unsharp masking. *IEEE Trans. Image Process.* **2000**, *9*, 505–510. [CrossRef] [PubMed]
22. Foroosh, H.; Zerubia, J.B.; Berthod, M. Extension of phase correlation to subpixel registration. *IEEE Trans. Image Process.* **2002**, *11*, 188–200. [CrossRef]
23. Bracewell, R.N. *The Fourier Transform and Its Applications*, 3rd ed.; McGraw-Hill: New York, NY, USA, 1999.
24. Sun, Z.; Tuitje, F.; Spielmann, C. A review of high-resolution microscopic ghost imaging with a low-dose pseudothermal light. *J. Microsc.* **2021**, *284*, 3–11. [CrossRef]
25. Chang, C.; Qi, Y.; Wu, J.; Xia, J.; Nie, S. Speckle reduced lensless holographic projection from phase-only computer-generated hologram. *Opt. Express* **2017**, *25*, 6568–6580. [CrossRef]
26. Johnson, D.H. Signal-to-noise ratio. *Scholarpedia* **2006**, *1*, 2088. [CrossRef]
27. Huynh-Thu, Q.; Ghanbari, M. Scope of validity of PSNR in image/video quality assessment. *Electron. Lett.* **2008**, *44*, 800–801. [CrossRef]
28. Wang, Z.; Bovik, A.C.; Sheikh, H.R.; Simoncelli, E.P. Image quality assessment: From error visibility to structural similarity. *IEEE Trans. Image Process.* **2004**, *13*, 600–612. [CrossRef] [PubMed]
29. Hou, G.; Pan, H.; Huang, B.; Wang, G.; Wei, W.; Pan, Z. Efficient L_1-based nonlocal total variational model of Retinex for image restoration. *J. Electron. Imaging* **2018**, *27*, 051207. [CrossRef]
30. Yuan, Y.; Shen, Y.; Peng, J.; Wang, L.; Zhang, H. Defogging Technology Based on Dual-Channel Sensor Information Fusion of Near-Infrared and Visible Light. *J. Sens.* **2020**, *2020*, 8818650. [CrossRef]
31. Sterczewski, L.A.; Westberg, J.; Wysocki, G. Computational coherent averaging for free-running dual-comb spectroscopy. *Opt. Express* **2019**, *27*, 23875–23893. [CrossRef]
32. Agaian, S.S.; Panetta, K.; Grigoryan, A.M. Transform-based image enhancement algorithms with performance measure. *IEEE Trans. Image Process.* **2001**, *10*, 367–382. [CrossRef] [PubMed]
33. Pizer, S.M.; Amburn, E.P.; Austin, J.D.; Cromartie, R.; Geselowitz, A.; Greer, T.; ter Haar Romeny, B.; Zimmerman, J.B.; Zuiderveld, K. Adaptive histogram equalization and its variations. *Comput. Vis. Graph. Image Process.* **1987**, *39*, 355–368. [CrossRef]
34. Abdullah-Al-Wadud, M.; Kabir, M.H.; Dewan, M.A.A.; Chae, O.; Kabir, H. A dynamic histogram equalization for image contrast enhancement. *IEEE Trans. Consum. Electron.* **2007**, *53*, 593–600. [CrossRef]
35. Khaleel, A.A. Dynamic Thermal Image Enhancement Using Wavelet-Based Adaptive Fusion. *Passer. J. Basic. Appl. Sci.* **2025**, *7*, 650–656. [CrossRef]
36. Jiao, L.; Wang, M.; Liu, X.; Li, L.; Liu, F.; Feng, Z.; Yang, S.; Hou, B. Multiscale deep learning for detection and recognition: A comprehensive survey. *IEEE Trans. Neural Netw. Learn. Syst.* **2024**, *36*, 5900–5920. [CrossRef] [PubMed]

37. Wu, Y.; Chen, Z.; Yi, W.; Yang, Y. MWA-Net: Multi-scale wavelet-guided attention network for single image dehazing. *Complex Intell. Syst.* **2025**, *11*, 449. [CrossRef]
38. Cvetkovic, S.D.; Schirris, J.; de With, P.H.N. Locally-adaptive image contrast enhancement without noise and ringing artifacts. In *Proceedings of the 2007 IEEE International Conference on Image Processing, San Antonio, TX, USA, 16–19 September 2007*; IEEE: New York, NY, USA, 2007; Volume 3, pp. III-557–III-560. [CrossRef]
39. Liu, Y.; Cui, G.; Shi, S.; Liao, F.; Cui, W.; Zhao, J. Improving the performance of speckle correlation imaging by using a speckle refinement method with self-calibrated homomorphic filtering. *Opt. Laser Technol.* **2024**, *179*, 111328. [CrossRef]
40. Cui, W.; Cui, G.; Liao, F.; Liu, Z.; Zhao, J. Noise-Resilient speckle imaging under illumination interference via row–column separated variational mode decomposition and principal singular value extraction. *Opt. Laser Technol.* **2025**, *192*, 113918. [CrossRef]
41. Konijnenberg, A.P.; Coene, W.M.J.; Pereira, S.F.; Urbach, H.P. Combining ptychographical algorithms with the Hybrid Input-Output (HIO) algorithm. *Ultramicroscopy* **2016**, *171*, 43–54. [CrossRef]
42. Idell, P.S.; Fienup, J.R.; Goodman, R.S. Image synthesis from nonimaged laser-speckle patterns. *Opt. Lett.* **1987**, *12*, 858–860. [CrossRef]
43. Guo, E.; Wei, Y.; Zhu, S.; Bai, L.; Han, J. Imaging of color targets through scattering media based on mixed speckle pattern separation. *Opt. Lasers Eng.* **2023**, *161*, 107324. [CrossRef]
44. Wu, T.; Guo, C.; Shao, X. Non-invasive imaging through thin scattering layers with broadband illumination. *arXiv* **2018**, arXiv:1809.06854. [CrossRef]

Disclaimer/Publisher's Note: The statements, opinions and data contained in all publications are solely those of the individual author(s) and contributor(s) and not of MDPI and/or the editor(s). MDPI and/or the editor(s) disclaim responsibility for any injury to people or property resulting from any ideas, methods, instructions or products referred to in the content.